From flapping to heaving:
a numerical study of wings in forward flight

A. Gonzalo[1], G.Arranz[1], M. Moriche[2], M. García-Villalba[1] & O. Flores[1]

[1] *Dept. Bioingeniería e Ing. Aeroespacial, Universidad Carlos III de Madrid, 28911 Leganés, Spain*
[2] *Inst. for Hydromechanics, Karlsruhe Institute of Technology, 76131 Karlsruhe, Germany*

Abstract

Direct Numerical Simulations of the flow around a pair of flapping wings are presented. The wings are flying in forward flight at a Reynolds number $Re = 500$, flapping at a reduced frequency $k = 1$. Several values of the radius of flapping motion are considered, resulting in a database that shows a smooth transition from the wing rotating with respect to its inboard wingtip (flapping), to a vertical oscillation of the wing (heaving). In this transition from flapping to heaving, the spanwise-averaged effective angle of attack of the wing increases while the effect of the Coriolis and centripetal accelerations becomes weaker. The present database is analyzed in terms of the value and surface distribution of the aerodynamic forces, and in terms of 2D and 3D flow visualizations. While the former allows a decomposition of the force in pressure (i.e., the component of the force normal to the surface of the wing) and skin friction (i.e., tangential to the surface of the wing), the latter allows the identification of specific flow structures with the corresponding forces on the wing. It is found that the aerodynamic forces in the vertical direction (lift) tend to increase for wings moving with larger radius of flapping motion, becoming maximum for the heaving configuration. This is mostly due to the increase of the spanwise-averaged effective angle of attack of the wing with the radius of the flapping motion. Also, the local changes in the effective angle of attack have a strong effect on the structure of the leading edge vortex, resulting in changes in the distribution of suction along the span near the leading edge of the wing. The effect of the apparent accelerations is mostly felt on the spanwise position where the separation of the LEV occurs. On the other hand, the differences in the force in the streamwise direction (thrust/drag) between the configurations with different radius of flapping motion seems to be linked to the position of the stagnation point dividing the suction and pressure side boundary layers, which seems to be controlled by the local effective angle of attack. Finally, the results of the DNS are used to evaluate the performance of an unsteady panel method, and to explain its deficiencies.

1 Introduction

Small flyers such as insects or small birds flap their wings to hover, fly forward, or perform maneuvers like take-off or perch. The desire to mimic the high-maneuverability of these flyers has guided the design of flapping-wing micro air vehicles (FWMAVs) [1]. The Reynolds number of operation of FWMAVs is in the range $10^2 - 10^4$, similar to that of insects or small birds [2]. For example, the Reynolds number of the fruit fly is $Re \sim 10^2$, and that of the Rufous hummingbird is $Re \sim 10^3$. Many studies have been conducted to increase the understanding of the aerodynamics of flapping wings at moderate and low Reynolds numbers, as reviewed by Shyy et al. [3]. However, although the unconventional aerodynamic mechanisms involved in the generation of forces by means of flapping wings (delayed stall of the leading edge vortex (LEV), rapid pitch up, wake capture and clap and fling) are known since the 1980s [4], it has been difficult to employ this knowledge to improve the systematic design of FWMAVs. Part of the problem is that the variety of maneuvers, wing kinematics and geometric parameters is so vast that there are no simple and reliable models for the aerodynamic forces covering this huge parametric space.

Since the problem is so complex, many studies have explored the simplified configuration of a heaving and/or pitching 2D airfoil [5, 6, 7, 8, 9, 10, 11]. Such studies have shown and quantified the role that the vortical structures formed during the oscillating cycle play in the process of force generation. In this simplified configuration, all sections of the corresponding *infinite* aspect ratio wing have an equal vertical displacement. However, this is not the case for natural flyers or FWMAVs that flap their wings so that the amplitude of motion increases from the wing root to

the wing tip. Thus, it seems of outmost importance to analyze the differences in the aerodynamic forces on a wing oscillating vertically (heaving) and a wing in a more realistic rotating motion (flapping). This question is explored in this manuscript by analyzing the transition from heaving to flapping for a pair of low-aspect ratio wings in forward flight, varying the radius of flapping motion from zero (flapping) to infinity (heaving).

A similar transition from a linear to an angular motion has been thoroughly studied in revolving wings [12, 13, 14, 15]. Compared to the kinematics of flapping wings, revolving wings only move in one direction (i.e., there is no stroke reversal). In those cases, the effect of the centripetal and Coriolis acceleration is to stabilize the LEV, producing an increase in lift as the radius of flapping motion decreases. In the literature of revolving wings, this effect is usually quantified with the Rossby number, which measures the ratio between the inertial force and the Coriolis force. A review of the recent literature on revolving wings is provided by Lee et al. [15], who emphasize the importance of both the Rossby number and the aspect ratio of the wing in order to characterize the aerodynamic forces of revolving wings.

The information concerning flapping wings in the forward flight regime is more scarce, apart from the particular case of heaving wings, reviewed by Gursul and Cleaver [16]. In recent years, flapping wings in forward flight have been studied by several authors, simulating both idealized configurations [17, 18, 19] as well as realistic configurations corresponding to insects [20, 21, 22, 23] birds [24], bats [25] and even micro air vehicles [26, 27]. While the emphasis in most of these studies lies in the characterization of the aerodynamic forces for the particular geometry or kinematics selected, few works analyze systematically the effect on the forces of varying kinematics or geometries. One of the exceptions is the work of Nagai et al. [20] who reported experiments and numerical simulations of an insect-like flapping wing, analyzing the effect on the aerodynamic forces of the position of the stroke plane and of the advance ratio. Another comprehensive study was performed by Bos et al [19]. They studied the effect of the radius of flapping motion on the aerodynamic forces, presenting an extensive database of cases in hover and a limited database of cases in forward flight. Their results show that both in hover and in forward flight, the aerodynamic force coefficients decrease as the radius of flapping motion increases, as a result of the stabilizing effect of the Coriolis and centripetal accelerations of the LEV. The most relevant for the present study is the work of Guerrero [18] who performed numerical simulations of a flapping, rectangular wing in forward flight. The author considered both heaving motion and a flapping motion with respect to the wing root at a Reynolds number of 250 based on the flight speed and wing chord. After analyzing the aerodynamic forces and flow visualizations, the author concluded that the heaving case produces larger forces and vortices than the flapping case, in apparent contradiction with the limited results reported by Bos et al [19] for forward flight.

In the present paper, we analyze the effect of the radius of flapping motion on the aerodynamic performance of a pair of flapping wings of small aspect ratio in forward flight. Several simulations are performed covering a parametric range between the cases of heaving motion and flapping motion with respect to the wing root. These two extreme cases are similar to the cases reported by Guerrero [18]. The paper is structured as follows. The description of the problem is provided in section 2. The numerical approach used to perform the numerical simulations is presented in section 3. The results are discussed in section 4. First the DNS results are discussed in terms of the aerodynamic forces over the wings. Then, the contributions from forces tangential and normal to the wing surface are analized, and related to the vortical structures appearing in the flow around the wing. Section 4 is closed with a comparison of the DNS results with an unsteady panel method. The conclusions of the study are presented in section 5.

2 Problem statement

The configuration considered in the present study consists of a pair of rectangular wings with an aspect ratio $AR = b/c = 2$, where c and b are the maximum chord and span of the wing, respectively. The wing cross-section is a NACA 0012 airfoil, which is a standard choice in the literature [28, 29]. The wings are flat, with no geometric twist, and rounded edges at the wing tips, as shown in Figure 1.

This pair of wings are placed side by side, as shown in Figure 1a, separated a distance $c/2$ (measured between the inboard wing tips). The wings perform a flapping motion (depicted in Figure 1b) as they fly forward at a constant speed u_∞. The flapping motion consists in a rotation of each wing around an axis parallel to the forward flight direction (red line in Figure 1b), which
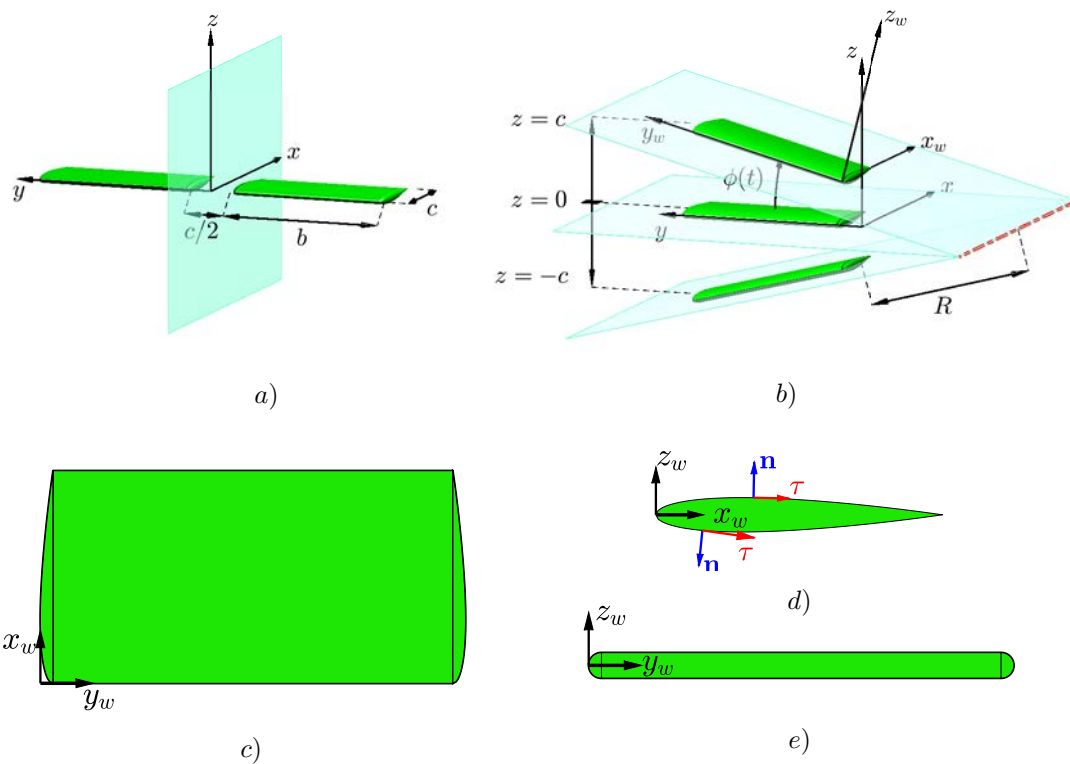
Figure 1: *a*) Sketch of the two wings configuration and *b*) sketch of the kinematics of the left wing. The wing chord, span of the wing and the radius of flapping motion, which is the distance between the inboard wing tip and the axis of rotation are denoted by *c*, *b* and *R*, respectively. *c*) Top view of the wing. *d*) Side view of the wing. *e*) Front view of the wing.

is located at a distance R from the inboard wing tip. The flapping angle, measured from the horizontal plane, follows a sinusoidal law,

$$\phi(t) = \phi_0 \cos(\omega t), \tag{1}$$

where ω is the angular frequency and ϕ_0 is the amplitude of the flapping motion. For all the simulations the vertical displacement of the outboard wing tip, h_0, has been kept fixed, $h_0 = c$, with the exception of one of the heaving wing simulations, as further discussed below. As a result, for the flapping wing simulations the amplitude of the flapping motion varies with the radius of flapping motion, R, as

$$\phi_0 = \arcsin\left(\frac{1}{R/c + AR}\right). \tag{2}$$

Note also, that since the vertical displacement of the outboard wing tip and the reduced frequency are the same for all cases, the vertical velocity of the outboard wing tip is approximately the same for any value of R. In particular, for the heaving case the vertical velocity of the outboard wing tip is

$$w_{tip}(t) = -h_0 \omega \sin(\omega t), \tag{3}$$

while for the flapping cases it becomes

$$w_{tip}(t) = (R + cAR)\cos(\phi)d\phi/dt = -\omega(R + cAR)\phi_0 \cos(\phi)\sin(\omega t). \tag{4}$$

Figure 1 also shows the two reference frames that will be used in the analysis of the results. First, an inertial reference frame x, y, z that moves with the wings at constant speed u_∞. In this reference frame, the forward motion results in an incoming free stream along the x (streamwise) direction. The vertical direction is z, and y is the direction along the span of the wing when $\phi(t) = 0$. Figure 1b shows a non-inertial reference frame, x_w, y_w, z_w, which moves with the wing so that x_w is the chordwise direction, y_w is the spanwise direction along the wing, and z_w is a direction perpendicular to the mean surface of the wing. The leading edge of the wing is at $x_w = 0$, and it moves due to the flapping motion in the $x = 0$ plane. The inboard wing tip of the wing is at $y_w = 0$, while the outboard wing tip is at $y_w/c = AR$.

As shown in Table 1, several values of R considered in the present study, varying from $R = 0$ (flapping with respect to the inboard wing tip, with $\phi_0 = 30°$) to $R \to \infty$ (heaving motion). For all cases, the reduced frequency is $k = \omega c/u_\infty = 1$ and the Reynolds number is $Re = u_\infty c/\nu = 500$, where ν is the kinematic viscosity. Note that, for completeness, the problem of a single wing in heaving motion has also been considered. This last case is labeled 1W-Rinf in Table 1, while the cases with two wings are labeled 2W-R### (with the last three digits corresponding to the numerical value of R/c). Additionally, a case of heaving motion with different amplitude of the vertical displacement of the outboard wing tip, h_0 equal to $0.52c$ has also been performed (2W-Rinf⋆).

As discussed in the introduction, the Rossby number is the ratio between the advective terms in the Navier-Stokes equations and the Coriolis accelerations. For flapping wings in forward flight with $h_0 = c$ this yields

$$Ro = \frac{u_\infty^2/c}{(\omega\phi_0)^2(R+b)} = \frac{1}{(k\phi_0)^2}\frac{c}{R+b} \approx \frac{1}{k^2}\left(AR + \frac{R}{c}\right), \tag{5}$$

where the last expression is an approximation for $R/c \gg 1$, where $\phi_0 \approx c/(R+b)$ (see equation 2). Since in the present study the reduced frequency is kept constant, $k = 1$, Ro varies only as a consequence of variations in the geometric parameters, as in [15]. Moreover, as the aspect ratio is $AR = 2$ for the cases presented, any increment in R/c is translated (almost) linearly into an increment in the Rossby number. Note also that, in the present configuration the choice of $k = 1$ results in u_∞ being of the same order of magnitude as the vertical velocity of the outboard wingtip, $\phi_0\omega(R+b)$, see eq. (4). Hence, the centripetal and the Coriolis accelerations are of the same order of magnitude for all cases in Table 1.

Finally, in order to keep the configuration as simple as possible, pitching motion of the wing has not been considered (i.e., rotation of the wing with respect to an axis parallel to y_w).

3   Numerical method

The problem described in the previous section is solved using Direct Numerical Simulations (DNS) with the in-house code TUCAN, which solves the Navier-Stokes equations for an incompressible flow. The presence of bodies of arbitrary shape (wings in this case) is modelled with the direct forcing Immersed Boundary Method (IBM) proposed by Uhlmann [30]. The fluid domain is discretized with a uniform, staggered Cartesian grid and centered, second-order finite differences are used to approximate the spatial derivatives. The time is discretized with a fractional-step method, in which the time advancement is performed with a low-storage Runge-Kutta scheme of three stages. The interested reader can find more details about TUCAN in [31, 32, 33].

In the present study, all the simulations with two wings (2W cases) are performed in a computational domain with dimensions $x = [-3c, 9c]$, $y = [0, 5.25c]$ and $z = [-4c, 4c]$ in the streamwise, spanwise and vertical directions, respectively. As shown in Figure 1a, $y = 0$ is the symmetry plane between both wings (indicated with a shaded plane), hence only the wing in the $y > 0$ domain is contained in the computational domain. The effect of the wing in the $y < 0$ domain is simulated by imposing a symmetry condition at the plane $y = 0$. Hence, the boundary conditions in the computational domain are uniform free stream at the plane $x = -3c$, outflow (advective) boundary condition at $x = 9c$, and free slip at the vertical ($z = -4c$, $z = 4c$) and spanwise ($y = 0$, $y = 5.25c$) boundaries.

Note that, even for completely symmetrical configurations, lateral instabilities might develop in the flow if the Reynolds number is sufficiently large, leading to non-symmetric aerodynamic forces on the wing [34]. As a consequence, the assumption of a symmetry condition at the center plane of the configuration is commonly used in the literature only for low to moderate Reynolds numbers [35, 36, 37]. For instance, Visbal et al.[37] simulated the flow around a heaving wing at $Re = 10000$ using an implicit LES and a symmetry condition at the mid-span of the wing. In the present case, the lower Reynolds number of the flow makes the assumption of symmetry with respect to $y = 0$ even more reasonable.

For the case with only one wing (1W-Rinf), the computational domain is $x = [-3c, 9c]$, $y = [-2c, 2c]$ and $z = [-4c, 4c]$ and $y = 0$ corresponds to the mid-span section of the wing. The boundary conditions are the same as in the 2W cases. Note that, even if this case is solved without the symmetry assumption, the resulting flow is completely symmetric with respect to the mid-span of the wing (not shown). This result supports the validity of the assumption of symmetry with respect to the plane $y = 0$ for the 2W cases.

The resolution employed in all computations is 56 grid points per chord length in all spatial directions ($\Delta x = \Delta y = \Delta z = c/56$). This resolution, which is comparable to that used in previous studies at similar Re [38], was chosen after a grid convergence study performed for a 2D airfoil in heaving motion at $Re = 500$ and $k = 1$ (see appendix). The total number of grid points of the computational domain for the 2W cases is $N_x = 672$, $N_y = 294$ and $N_z = 448$. For the case 1W-Rinf the resolution is the same, resulting in a lower number of grid points in the spanwise direction ($N_y = 224$). In addition to the grid for the fluid domain, a Lagrangian grid for the wing needs to be defined. In the IBM of Uhlmann [30], the area associated to each Lagrangian point has to be roughly the same as the square of the grid spacing for the fluid domain. This leads to a total number of 17,050 Lagrangian points evenly distributed on the surface of the wing.

All cases in Table 1 are simulated with the same initial condition, $u = u_\infty$ and $v = w = 0$ (i.e., unperturbed free-stream velocity). The simulations are run until the velocity field and the forces on the wing reach a periodic state, with period $T = 2\pi/\omega = 2\pi c/ku_\infty$, imposed by the motion of the wing. This periodic state is reached after a transient of approximately $10T$. The first four cycles are run with a lower resolution. Then, the velocity field is interpolated onto the fine grid, and run for another 6 cycles. Note that the aerodynamic forces converge after 2-3 cycles while the flow downstream of the airfoil needs a longer time integration interval to converge. After that transient, the variation in the aerodynamic forces or flow velocities between consecutive cycles are negligible (relative differences smaller than 10^{-5}).

It is important to take into account that one of the advantages of the algorithm implemented in TUCAN is that it provides directly the distribution of aerodynamic forces per unit area on the surface of the wing, $\mathbf{f}$. This feature was exploited by Chan-Braun et al. [39] to analyze the hydrodynamic force distribution on the surface of spherical particles in a low-Reynolds number turbulent flow and by Arranz et al. [40] to analyze the force distribution on the wing of a winged-seed in autorotation. In the present study, the force per unit area is decomposed during postprocessing as

Cases	R/c	Ro	ϕ_0	h_0/c	$\langle\alpha_e\rangle_{\max}$	$\overline{C_x}$	$\overline{C_z}$	$\overline{C_{My}}$
2W-R000	0.0	1.82	30.00°	1.00	27.64°	0.143	0.859	-0.258
2W-R005	0.5	2.36	23.58°	1.00	31.69°	0.132	1.052	-0.319
2W-R020	2.0	3.92	14.48°	1.00	37.16°	0.115	1.356	-0.420
2W-R080	8.0	9.97	5.74°	1.00	42.03°	0.094	1.670	-0.531
2W-Rinf	∞	∞	-	1.00	45.00°	0.080	1.888	-0.615
1W-Rinf	∞	∞	-	1.00	45.00°	0.081	1.808	-0.579
2W-Rinf⋆	∞	∞	-	0.52	27.64°	0.142	0.877	-0.251

Table 1: Parameters and main results of DNS cases simulated. R is the radius of flapping motion, Ro is the Rossby number (see equation 5), ϕ_0 is the amplitude of the flapping angle (in degrees), h_0 is the amplitude of the vertical displacement of the outboard wing tip and $\langle\alpha_e\rangle_{\max}$ is the maximum absolute value of the effective angle of attack averaged along the wing span (in degrees), which occurs at mid-stroke. The coefficients $\overline{C_x}$, $\overline{C_z}$ and $\overline{C_{My}}$ are the streamwise force coefficient, the vertical force coefficient and the pitching moment coefficient with respect to the leading edge of the wing, respectively. All three coefficients are time-averaged during the downstroke of the wing.

the sum of two vectors, namely, a vector normal to the surface and a vector tangent to the surface,

$$\mathbf{f}_{n*} = (\mathbf{f}\cdot\mathbf{n})\,\mathbf{n} \qquad \text{and} \qquad \mathbf{f}_\tau = \mathbf{f} - \mathbf{f}_{n*}. \tag{6}$$

Note that $\mathbf{n}$ is the local unit vector normal to the surface, pointing towards the fluid, as shown in Figure 1d. Note that from a physical point of view, $\mathbf{f}_{n*}$ corresponds to the forces due to the pressure and the normal viscous stresses, while $\mathbf{f}_\tau$ corresponds to the skin friction (i.e. the tangential shear stresses acting on the surface of the wing). Finally, for convenience we also define

$$\mathbf{f}_n = \mathbf{f}_{n*} - \left(\frac{1}{S}\int_S (\mathbf{f}\cdot\mathbf{n})\,\mathrm{d}S\right)\mathbf{n}, \tag{7}$$

where S stands for the wetted surface of the wing. Note that (7) is roughly equivalent to removing the ambient pressure from $\mathbf{f}_{n*}$. In any case, the differences between $\mathbf{f}_n$ and $\mathbf{f}_{n*}$ are small, less than 10%. Note also that the total force resulting from integrating $\mathbf{f}_n$ and $\mathbf{f}_{n*}$ over the (closed) surface of the wing is exactly the same.

Finally, the IBM used to simulate the presence of the moving wing has limitations to describe the force distribution near the trailing edge (TE) of the wing. Such limitations have been recently addressed by Maertens and Weymouth [41], though not implemented in this study. The problem arises due to the discrete representation of the Dirac's delta employed to transfer the forces from the wing's grid to the mesh where the fluid is solved (regularized delta functions, see [42]). In the present calculations, we use a 4-point regularized delta function, which introduces a spurious interaction between the upper and lower surfaces of the wing when the distance between them is smaller than $2\Delta x$. For the present geometry and resolution, this corresponds to $x_w \gtrsim 0.85c$. In this region (indicated with a dashed line in the force distributions shown in Figures 5 and 9) the distributions of $\mathbf{f}, \mathbf{f}_\tau$ and $\mathbf{f}_n$ are not reliable. However, the spurious interactions between the upper and lower surface cancel each other, so that the total force (integrated over the whole wing) is not affected by this phenomenon [31, 32, 33].

4 Results

4.1 Aerodynamic forces

Figure 2 shows the time evolution of the net force coefficients,

$$C_x = \frac{1}{\frac{1}{2}\rho u_\infty^2 bc}\int_S \mathbf{f}\cdot\mathbf{e}_x\mathrm{d}S, \qquad\qquad C_z = \frac{1}{\frac{1}{2}\rho u_\infty^2 bc}\int_S \mathbf{f}\cdot\mathbf{e}_z\mathrm{d}S, \tag{8}$$

where ρ is the density of the fluid, $\mathbf{e}_x$ and $\mathbf{e}_z$ are the unit vectors in the streamwise (x) and vertical (z) directions, respectively. The corresponding time-averaged force coefficients during the

downstroke (i.e., half cycle) are reported in Table 1 ($\overline{C_x}$ and $\overline{C_z}$). The pitching moment coefficient is defined as

$$C_{My} = \frac{1}{\frac{1}{2}\rho u_\infty^2 bc^2} \int_S (\mathbf{x}_P \times \mathbf{f}) \cdot \mathbf{e}_{y_w} \mathrm{d}S, \tag{9}$$

where $\mathbf{x}_P$ is the position vector of any point of the wing surface with respect to the leading edge and $\mathbf{e}_{y_w}$ is the unit vector along the wing span. For completeness, we also include in Table 1 the values of $\overline{C_{My}}$, the pitching moment coefficient averaged over half cycle.

Due to the vertical symmetry of the motion, the vertical force (Figure 2a) generated during the downstroke is equal in magnitude to the vertical force generated during the upstroke, but with opposite sign. With increasing radius of flapping motion, the peak of C_z increases, so that the maximum force is obtained for the heaving wing case, 2W-Rinf. Interestingly, case 1W-Rinf has peak values of C_z slightly lower than case 2W-Rinf. Note also, that the peak is reached slightly before the mid-downstroke for all cases shown in Figure 2a, at a time that does not seem to depend on R.

While for the present configuration the peak of C_z increases with R, a different trend has been reported for revolving wings [12, 13, 14, 15]. These studies found that the maximum of C_z is greater for wings rotating with smaller R, and this result was attributed to a stabilization of the LEV produced by the Coriolis force. The reason behind this discrepancy might be found in a fundamental difference concerning the effective angle of attack of the wing, α_e, in revolving wings with respect to the present configuration. In revolving wings, the effective angle of attack is just the geometrical angle of attack of the wing, constant for all spanwise positions and independent of R. For flapping wings in forward flight, the effective angle of attack is given by the ratio of the vertical velocity at each spanwise section, $w_w(y_w, t)$, and the forward flight velocity, resulting in

$$\alpha_e(y_w, t) = \arctan\left(\frac{w_w(y_w, t)}{u_\infty}\right) = \arctan\left(\frac{(R + y_w)d\phi/dt}{u_\infty}\right). \tag{10}$$

It is also useful to define the effective angle of attack averaged over the wing span

$$\langle\alpha_e\rangle(t) = \frac{1}{b} \int_0^b \alpha_e(y_w, t)\mathrm{d}y_w. \tag{11}$$

Hence, for a constant value of h_0 the flapping wing moves faster as R increases, resulting in larger $\langle\alpha_e\rangle$ (see Table 1), and larger C_z during the downstroke. Recall that, by design the vertical velocity of the outboard wing tip is approximately the same for the cases with $h_0 = c$, (see equations 3-4) and therefore α_e is roughly independent of R at the outboard wing tip. When $R \to \infty$, both $w_w(y_w, t)$ and $\alpha_e(y_w, t)$ become uniform over the wing, maximizing the aerodynamic force. Hence, we hypothesize that the larger α_e along the wing span is responsible for the increase of C_z with R.

In order to confirm this hypothesis, we have performed an additional simulation in heaving motion, case 2W-Rinf*. The heaving amplitude, $h_0/c = 0.52$, has been selected so that the effective angle of attack of the wing is the same as the spanwise-averaged effective angle of attack of the case with $R = 0$ (case 2W-R000), see Table 1. The profiles of C_z as a function of time for both cases (2W-R000 and 2W-Rinf*) are shown in Figure 2a. They are found to be very similar, with a small variation of the peak values and the time when they are reached. Thus, it is confirmed that for the present configuration the variation of the aerodynamic forces with R is mainly governed by the resulting variation of the effective angle of attack, with little influence of Ro (i.e., inertial terms seem to be dominant over the apparent acceleration terms). Note that the value of $\overline{C_z}$ reported in Table 1 for 2W-R000 is marginally smaller (about 2%) than for 2W-Rinf*. Although this difference might be too small to be significant in the present case, it is qualitatively consistent with the results of Guerrero [18], who reported larger aerodynamic forces for heaving wings than for flapping wings, at a somewhat lower Re and higher k than the present cases.

In terms of the forces in the streamwise direction (Figure 2b), the evolution of C_x is the same during the upstroke and during the downstroke, owing to the symmetry of the motion. For all cases, the values of C_x during the downstroke/upstroke are essentially positive, indicating that net drag is being produced. This result indicates that the wing kinematics employed in this study should not have practical utility to sustain forward flight. However, as mentioned above, the kinematics do illustrate the effect of R in a configuration as simple as possible.

Figure 2b also shows that the maximum value of C_x is reached during the transitions between upstroke and downstroke, around $t/T = 0$ and 0.5. The dependence of the peak values of C_x with
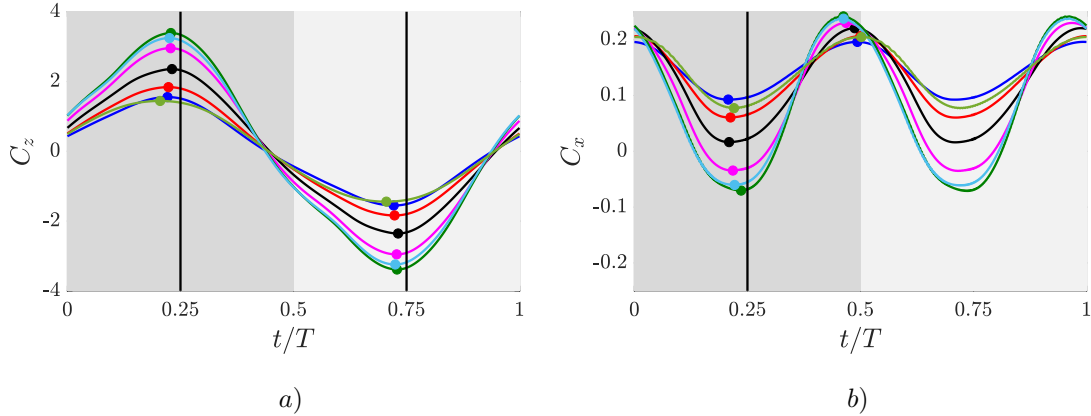
Figure 2: Forces coefficients a) C_z and b) C_x during one cycle of DNS cases 2W-R000 (⎯⎯), 2W-R005 (⎯⎯), 2W-R020 (⎯⎯), 2W-R080 (⎯⎯), 2W-Rinf (⎯⎯), 1W-Rinf (⎯⎯) 2W-Rinf* (⎯⎯). Maximum and minimum values of the forces coefficients are depicted with (●). Dark and light greys regions represent downstroke and upstroke motions respectively.

R is weak for the cases with the same h_0, and the magnitude ($C_{x,\mathrm{max}} \approx 0.2$) is similar to the drag coefficient of a rectangular flat plate of $AR = 2$ at zero angle of attack and a comparable Reynolds number, $Re = 300$ [38]. However, the time to $C_{x,\mathrm{max}}$ varies significantly with R for these cases, although it remains close to $t/T = 0$ and 0.5 for all cases. On the other hand, the minimum value of C_x (i.e., when the wing is closer to produce thrust) is obtained at the mid-downstroke and mid-upstroke, $t/T = 0.25$ and 0.75, when the effective angle of attack is maximum over the wing. The effect of R in the magnitude of $C_{x,\mathrm{min}}$ is apparent for the cases with the same h_0. Indeed, cases 2W-R080 and 2W-Rinf show negative values of C_x at mid-upstroke and mid-downstroke, indicating thrust production.

Finally, note that, for the cases with the same $\langle \alpha_e \rangle$, 2W-R000 and 2W-Rinf*, the differences between the peaks of C_x are similar to those found in C_z, even if the time-averaged streamwise force during the downstroke motion ($\overline{C_x}$) of both cases is roughly the same (see Table 1). At the mid-downstroke ($t/T = 0.25$), the minimum of C_x is larger for 2W-Rinf* than for 2W-R000, indicating less drag production. Interestingly, for these two cases that isolate the effect of R from the effect of the effective angle of attack, the trend of $C_{x,\mathrm{min}}$ with R is the same as that found for the cases with $h_0 = c$. This suggests that the effect of both R and α_e is to produce more negative streamwise forces, i.e. less drag or more thrust.

In order to evaluate the origin of the changes in C_z and C_x at mid-stroke (more lift and more thrust as R and $\langle \alpha_e \rangle$ increase), the contributions from the normal and tangential forces to C_x and C_z are analyzed next. These contributions are defined as

$$C_i^n = \frac{\int_S \mathbf{f}_n \cdot \mathbf{e}_i \mathrm{d}S}{\frac{1}{2}\rho u_\infty^2 bc}, \qquad C_i^\tau = \frac{\int_S \mathbf{f}_\tau \cdot \mathbf{e}_i \mathrm{d}S}{\frac{1}{2}\rho u_\infty^2 bc}, \qquad (12)$$

where the subindex i stands for x or z. Recall that, from a physical point of view, C_i^n is related to the pressure forces mainly, while C_i^τ is the contribution from the viscous skin friction.

Although not shown, C_z is dominated by the contribution from the normal force (i.e., pressure forces), while the contribution from tangential forces is smaller than 13% in all cases. In other words, pressure is dominant in the generation of lift. On the other hand, the contribution of normal and tangential forces to C_x is more balanced. This can be observed in Figure 3 where the time history of C_x^n and C_x^τ are shown for all the 2W cases. The contribution of C_x^n (Figure 3a) corresponds to thrust during most of the cycle, while the contribution of C_x^τ (Figure 3b) always corresponds to drag. This suggests that the pressure forces are responsible for the lift and the thrust contributions generated by the wing during the downstroke. The thrust provided by the normal forces increases with $\langle \alpha_e \rangle$, the same as C_z in Figure 2a. Note that the two cases with different R but same $\langle \alpha_e \rangle$ have roughly the same C_x^n, suggesting that the effect of R on the surface integral of the pressure forces is limited in the present cases.
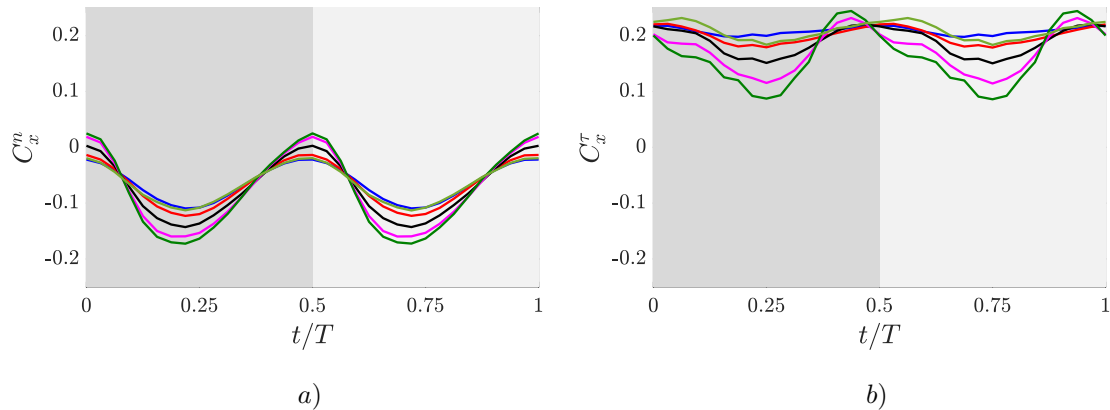
8

Figure 3: Streamwise force coefficient a) normal (C_x^n) and b) tangential (C_x^τ) components during one cycle of 2W cases 2W-R000 (——), 2W-R005 (——), 2W-R020 (——), 2W-R080 (——), 2W-Rinf (——) and 2W-Rinf* (——). Dark and light greys regions represent downstroke and upstroke motions respectively. Note that the vertical scale has been chosen so that Figures can be compared with Figure 2b

Interestingly, the contribution from the skin friction to the drag is larger for case 2W-R000, which shows in Figure 3b a fairly constant value of C_x^τ over the whole cycle. The time-averaged C_x^τ of cases 2W-R000 and 2W-Rinf* are almost the same, although the instantaneous values of C_x^τ of the latter present stronger oscillations than the former. In the cases with $h_0 = c$, as $\langle \alpha_e \rangle$ increases, C_x^τ decreases during both the downstroke and the upstroke. Indeed, the effect of $\langle \alpha_e \rangle$ on the contribution from the tangential forces seems to be larger than in the contribution from the normal forces, with absolute variation between 2W-Rinf and 2W-R000 of 0.11 and 0.06 for C_x^τ and C_x^n, respectively. Finally, it is interesting to note that the dependence of the time to $C_{x,\max}$ with $\langle \alpha_e \rangle$ is associated to the tangential force contribution (compare Figures 2a and 3b around $t/T = 0$ and 0.5).

4.2 Tangential force distribution

The analysis of C_i^n and C_i^τ in the previous section seems to suggest that R and $\langle \alpha_e \rangle$ affect differently normal (pressure) and tangential forces (skin friction). In this subsection, we focus in the latter, specifically in the contributions to C_x^τ from the different parts of the wing. To that end, we define

$$c_x^\tau(x_w) = \frac{1}{bc} \int_0^b \int_0^{x_w} c_\tau(\xi, \eta) \, \boldsymbol{\tau} \cdot \mathbf{e}_x \mathrm{d}\xi \mathrm{d}\eta, \qquad (13)$$

where $\boldsymbol{\tau}$ is a local unit vector tangent to the wing surface pointing towards the streamwise direction, as shown in Figure 1d, x_w is the chordwise coordinate on the reference frame of the wing and $c_\tau(x_w, y_w)$ is the local tangential force coefficient on the wing surface, defined as

$$c_\tau = \frac{\mathbf{f}_\tau \cdot \boldsymbol{\tau}}{\frac{1}{2}\rho u_\infty^2}. \qquad (14)$$

Note that the surface integral in (13) extends over the whole span of the wing, and from the leading edge to the chordwise coordinate x_w both over the upper and lower surfaces of the wing. From a physical point of view, $c_x^\tau(x_w)$ is the contribution to C_x^τ from the surface of the wing located between the leading edge and the chordwise coordinate x_w, so that $c_x^\tau(c) = C_x^\tau$.

Figure 4a shows $c_x^\tau(x)$ at the mid-downstroke ($t/T = 0.25$), the time instant when the differences in C_x^τ in Figure 3 are maxima. Near the leading edge of the wing, c_x^τ presents a minimum for all the cases. This peak value decreases with R for all the cases with the same h_0 and is similar for the cases with the same α_e (2W-R000 and 2W-Rinf*). After that minimum, c_x^τ grows with x_w at a similar rate for all the cases. This suggests that the differences in C_x^τ observed in Figure 3b are mainly due to the behaviour of the flow close to the leading edge of the wing.
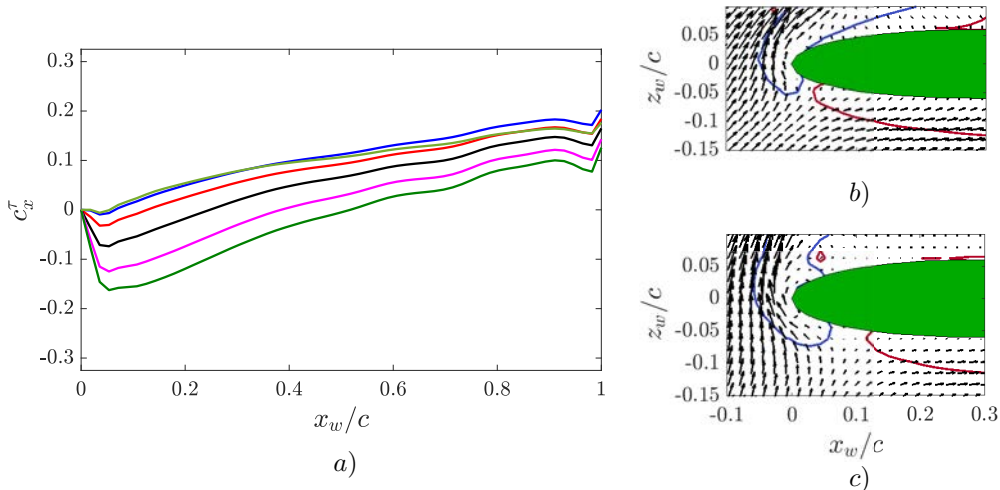
Figure 4: *a*) Streamwise contribution of the local tangential force coefficient (c_τ) to C_x^τ as a function of x_w at the mid-downstroke ($t/T = 0.25$). 2W-R000 (——), 2W-R005 (——), 2W-R020 (——), 2W-R080 (——), 2W-Rinf (——) and 2W-Rinf* (——). *b*) and *c*) relative velocity field at the wing span section $y_w/b = 0.5$ for cases 2W-R000 and 2W-Rinf, respectively. Two spanwise vorticity contour lines ($\omega_y c/u_\infty = 5$ and $\omega_y c/u_\infty = -5$) are shown in blue and red respectively. The wing section is displayed in green.

In order to evaluate the origin of these negative contributions to C_x^τ (i.e., thrust due to skin friction) near the leading edge of the wing, Figures 4*b* and 4*c* show the relative velocity at the mid-span of the wing at mid-downstroke for cases 2W-R000 and 2W-Rinf, respectively. In both Figures the stagnation point can be identified in the pressure side of the wing, in the region between the two spanwise vorticity contour lines shown in blue (clockwise) and red (anticlockwise). These plots show that the negative peak of $c_x^\tau(x_w)$ for $x_w \lesssim 0.1c$ is due to the skin friction of the boundary layer developing from the stagnation point to the leading edge of the wing. Since the stagnation point is located further away from the leading edge for the case 2W-Rinf than for case 2W-R000, the minimum of $c_x^\tau(x_w)$ of the former has a larger absolute value than the latter. Although not shown here, the stagnation point for the heaving case (2W-Rinf*) with equal $\langle \alpha_e \rangle$ than 2W-R000 is located at the same x_w than the latter, resulting in a similar magnitude of the negative peak in $c_x^\tau(x_w)$ in Figure 4*a*. Therefore, independently of R, the results shown in Figure 4 suggest that in sections with larger α_e, the flow moves faster around the leading edge (from the pressure side to the suction side), generating more thrust. This faster flow also results in a normal suction force at the leading edge, which will be discussed below.

4.3   Normal force distribution

We now turn our attention to the vertical force. Unlike the streamwise force, the vertical force is dominated by the contribution of the normal force, which represents almost 90% of the total C_z in the cases studied here. Thus, in order to better characterize the combined effect of R and α_e on C_z, the distribution of the normal force on the surface of the wing is analyzed first. This distribution is studied in the lower and upper surfaces separately, to allow the detailed analysis of the effect of the LEV on C_z. First, the local normal force coefficient given by

$$c_n = \frac{\mathbf{f}_n \cdot \mathbf{n}}{\frac{1}{2}\rho u_\infty^2},\tag{15}$$

is characterized at the mid-downstroke ($t/T = 0.25$, see Figure 5), approximately when aerodynamic forces are maxima. Note that c_n is analogous to the (minus) pressure coefficient: positive c_n corresponds to suction, which results in positive contributions to the lift in the upper surface and negative contributions to the lift in the lower surface.
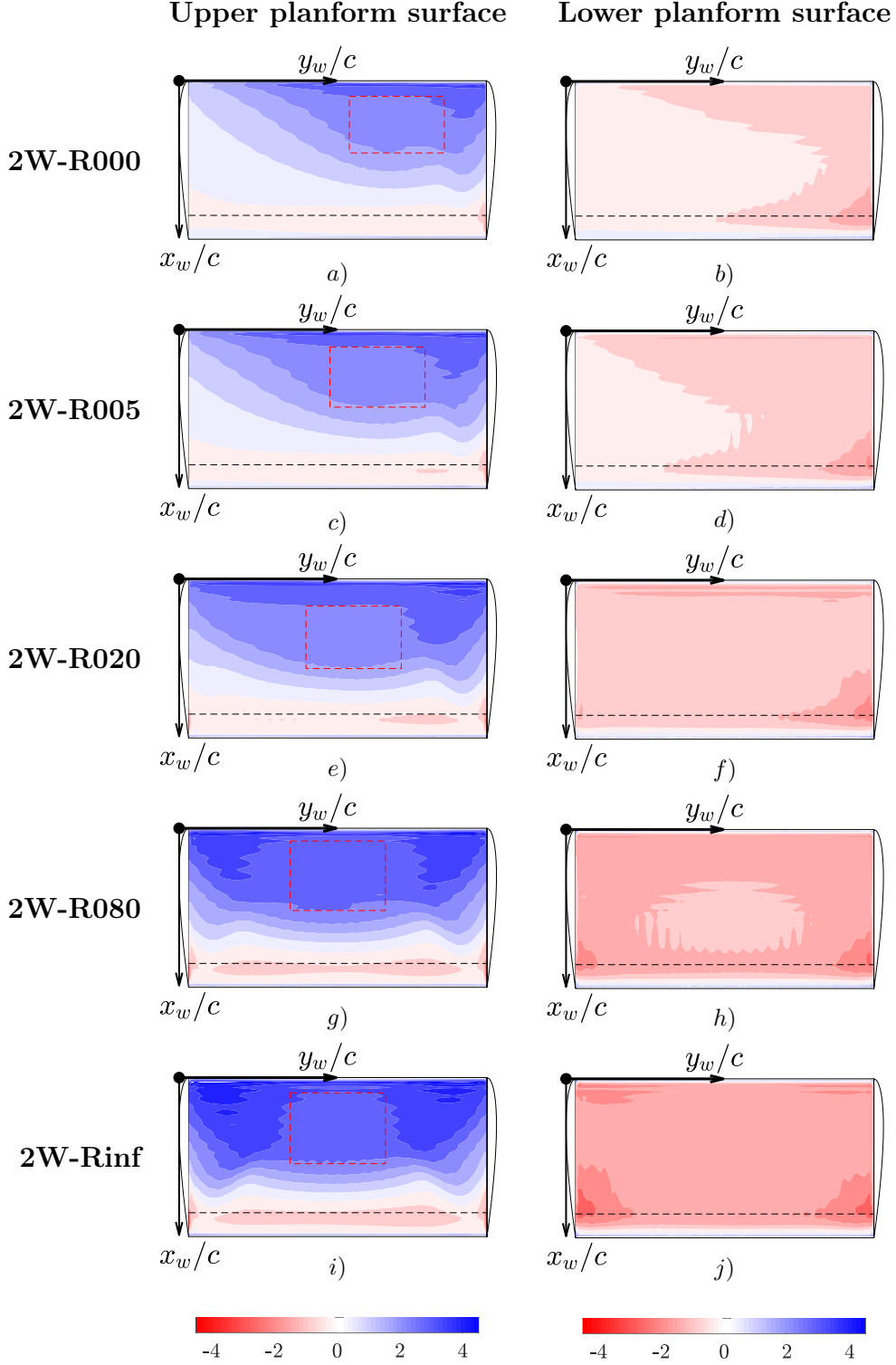
Upper planform surface — Lower planform surface

2W-R000 — a) b)

2W-R005 — c) d)

2W-R020 — e) f)

2W-R080 — g) h)

2W-Rinf — i) j)

Figure 5: Distribution of the local normal force coefficient (c_n) at the mid-downstroke. (a), (c), (e), (g), (i) upper surface. (b), (d), (f), (h), (j) lower surface. (a)-(b) Case 2W-R000. (c)-(d) Case 2W-R005. (e)-(f) Case 2W-R020. (g)-(h) Case 2W-R080. (i)-(j) Case 2W-Rinf. The red dashed rectangle indicate approximately the regions where $\partial_x c_n \approx 0$. The black dashed line at $x/c = 0.85$ limits the region where the IBM is not providing an accurate description of c_n, as discussed in section 3.

The c_n distributions displayed in Figure 5 show that suction is dominant in the upper surface, while positive pressure (i.e., negative c_n) is dominant in the lower surface. Very close to the leading edge, c_n tends to be positive both in the upper and lower surface, which explains the negative sign of C_x^n (thrust) in Figure 3a at mid-downstroke. This is the so-called suction force in potential theory. Near the trailing edge, the sign of c_n tends to change. Note however that this occurs in the region where the distance between the upper and lower surface is too small for the IBM to provide accurate surface distributions of the force (as discussed in section 3).

For $R \to \infty$ (2W-Rinf, see Figure 5i and j), the c_n distribution is roughly symmetric with respect to the mid-span of the wing. In the cases with $h_0 = c$, the magnitude of c_n in the inboard wing tip ($y_w = 0$) decreases with R, resulting in a force distribution along the spanwise direction that peaks near the outboard wing tip ($y_w = b$). Indeed, the local normal force distribution near the outboard wing tip is qualitatively the same in these five cases, although the intensity of the suction peak in the upper surface slightly increases with R. This is consistent with the variation of the local α_e, decreasing with R towards the inboard wing tip while remaining constant at the outboard wing tip. The c_n distribution in the lower surface is more uniform than over the upper surface, although the effect of α_e on the spanwise distribution of c_n is clearly discernible too. Note that, besides the apparent differences in the c_n distribution in the upper and lower surfaces, both surfaces of the wing contribute in a similar percentage to C_z.

Finally, Figure 5 shows that $\partial c_n / \partial x_w \lesssim 0$ over the upper surface, which is consistent with an adverse pressure gradient (as typically observed in the suction side of wings). As R decreases, this adverse pressure gradient is relieved in the region close to the inboard wing tip, where the effective angle of attack becomes smaller. Besides that, all cases shown in Figure 5 exhibit a region with $\partial c_n / \partial x_w \approx 0$ on the upper surface of the wing (i.e., the region where the x_w distance between consecutive iso-lines of c_n is larger, highlighted with a red dashed rectangle in Figure 5). This region is located around the mid-span of the wing for case 2W-Rinf, but moves towards the outboard wing tip as R decreases. The fact that $\partial c_n / \partial x_w \approx 0$ could be an indicator of the presence of a stagnation region where the boundary layer is separated or the flow is recirculating. In the lower surface of the wing, the chordwise gradients of c_n are smaller but positive, resulting in a slightly favorable pressure gradient in most of the wing (except near the wing tips), showing no indication of separation of the boundary layer.

These interpretations of the distributions of c_n over the upper surface of the wing are supported by flow visualizations, like those presented in the supplementary videos, and in Figure 6 for the mid-downstroke of all cases with $h_0 = c$. The left row of panels in Figure 6 shows vortical structures, identified using two iso-surfaces of the second invariant of the velocity gradient tensor Q, namely the Q-criterion of Hunt et al [43]. The two iso-surfaces of Q shown in the Figure correspond to $Q = \sigma/8$ (light blue) and $Q = \sigma/4$ (dark blue), where σ is the standard deviation of Q calculated in a box of size $2.5c \times 4.5c \times 3c$, centered at $x_w/c = 0.5$ and $y_w/c = z_w/c = 0$. Note that the value of Q can be interpreted as a measure of the intensity of the vortex, hence light blue structures correspond to weak vortices, while dark blue structures (surrounded by a light blue iso-surface) correspond to intense vortices. The central and right rows of the Figure show the spanwise vorticity (ω_{y_w}) at two x_w-z_w planes, $y_w/b = 0.5$ (mid-span) and $y_w/b = 0.75$ (closer to the outboard wing tip), respectively. For reference, these x_w-z_w cuts also include the iso-contours of $Q = \sigma/4$, plotted in dark blue in the left row. Note that positive ω_{y_w} (blue) corresponds to clockwise rotating vortices.

The overall evolution of the vortices in the upper and lower surfaces of the wings can be observed in the videos provided in the supplementary material. As the downstroke begins, a strong LEV forms in the upper surface of the wing, flanked by wing tip vortices. The structure of these vortices at mid-downstroke ($t/T = 0.25$) can be observed in the left row of Figure 6. The wing-tip vortices are very clear in the outboard wing tip of the five cases, but their intensity (i.e., volume of the Q iso-surfaces) in the inboard wing tip quickly decreases with R, due to the reduced pressure difference between the pressure and suction sides in that region (i.e., see c_n distributions near the inboard wing tip in Figure 5). At or close to the stroke reversal ($t/T = 0.5$), the LEV and the tip-vortices are shed into the wake, generating the ring-like structures that can be observed in the wakes shown in the left row of Figure 6. These ring-like vortices are very similar to those reported in previous works [18, 44, 45]. For relatively large radius of flapping motion, $R/c \gtrsim 2$, these ring-like vortices are quite symmetric (see Figures 6g, j and m), becoming less clear for 2W-R005 and 2W-R000.

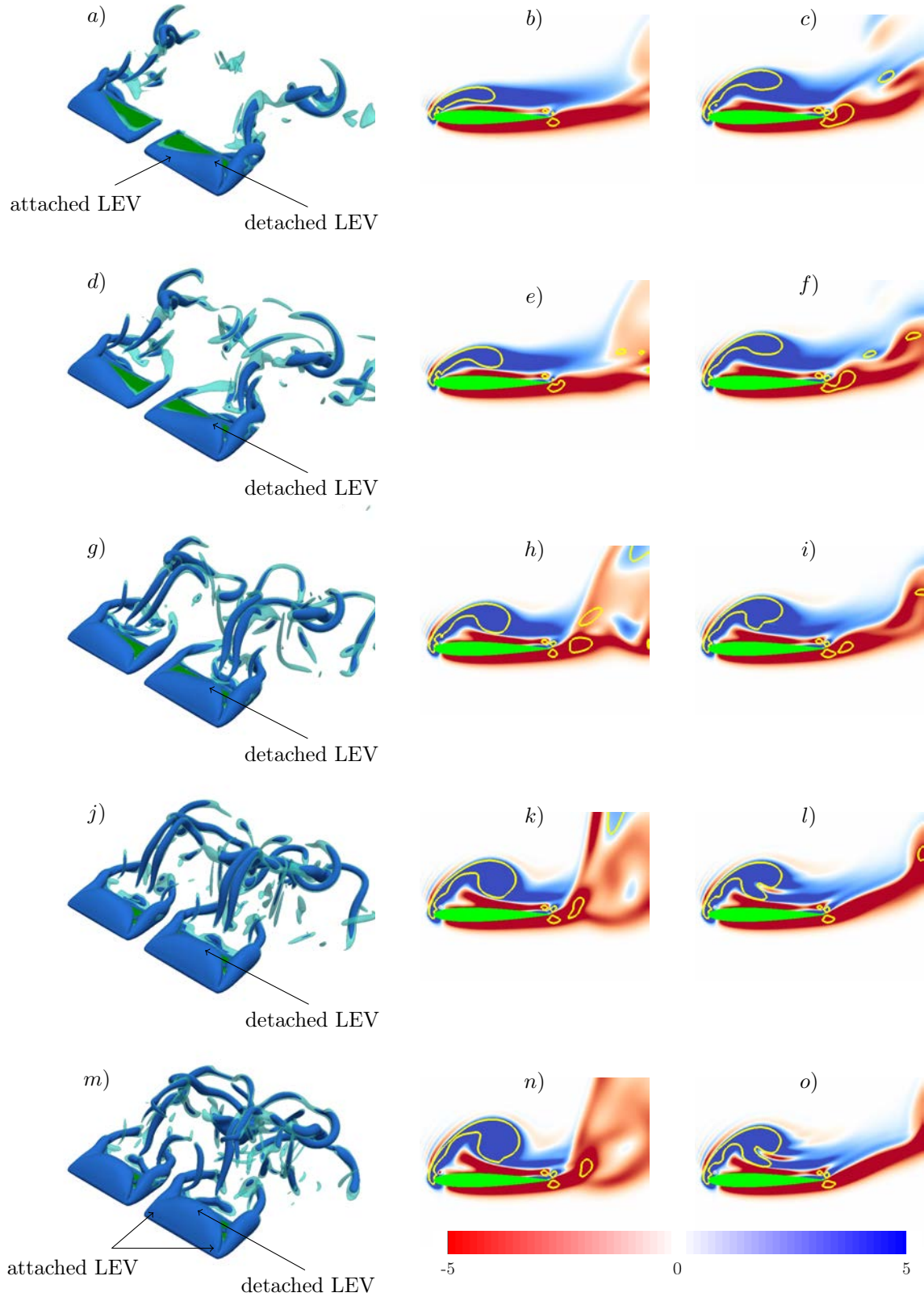Besides the wing-tip vortices of the inboard wing tip and the ring-like structures in the wake,

Figure 6: Flow visualization at $t/T = 0.25$ of cases 2W-R000 (a, b, c), 2W-R005 (d, e, f), 2W-R020 (g, h, i), 2W-R080 (j, k, l) and 2W-Rinf (m, n, o). In the left panels two different iso-surfaces of $Q = \sigma/8$ (light blue) and $Q = \sigma/4$ (dark blue) are shown. In the central panels, x_w-z_w cuts of the spanwise vorticity at $y_w/b = 0.5$ are shown in a red-blue colormap, while the right panels correspond to cuts at $y_w/b = 0.75$. The yellow line represents the x_w-z_w cut of the dark blue iso-surface of Q shown in the left panels. Wings are displayed in green in this Figure.

the radius of flapping motion R and the spanwise-averaged effective angle of attack $\langle \alpha_e \rangle$ have a strong influence on the structure of the LEV. At the mid-downstroke, the left row of Figure 6 shows that the LEV becomes less intense (i.e., smaller volume in the Q iso-surface) in the inboard side of the wing as R and the local α_e decrease. However, its structure near the outboard wing tip, where the local α_e is similar for the cases with $h_0 = c$, remains practically unchanged. This variation is qualitatively similar to that reported in previous works for revolving wings [46, 14, 47, 48, 49].

The weakening of the LEV in the inboard wing tip for cases with small R is consistent with the distribution of $\alpha_e(y_w, t)$. It also correlates with the evolution of the c_n distributions in the upper surface of the wing (Figure 5). This is indeed expected, since previous studies have associated the suction peaks near the leading edge to the LEV [50, 51, 52]. For the present cases, the x_w-z_w cuts shown in Figure 6 together with the supplementary videos show that the LEV is indeed being shed into the wake shortly after the mid-downstroke, and that the region where this occurs moves towards the outboard wing tip as R decreases (i.e. where the local α_e is higher). For instance, it is possible to observe in Figure 6k and n that cases 2W-R080 and 2W-Rinf have a separated LEV at mid-span, in the sense of having an LEV relatively far from the wing surface. However, at the same spanwise section, Figure 6b shows a developing LEV for case 2W-R000, which could be considered to be attached (i.e., closer to the wing surface). Closer to the outboard wing tip, at $y_w/b = 0.75$ (see Figure 6c), the LEV is located further away from the wing surface, with a distribution of vorticity beneath the vortex similar to that shown in Figure 6k and 6n, suggesting that the LEV is separated. Although not shown, closer to the outboard wing tip, the contours of Q become closer to the surface of the wing, suggesting that the LEV remains anchored to the wing in that region. Indeed, the left row of Figure 6 and the movies on the supplementary material seem to suggest that the tip vortices, when present, act as an anchoring structure for the LEV, as suggested by Birch & Dickinson [53]. Summarizing, the LEV separates at the mid-span for $R \to \infty$, while separation occurs closer to the outboard wing tip as R decreases.

After analyzing qualitatively the influence of R and $\langle \alpha_e \rangle$ on the LEV separation and how it correlates with the normal force distribution on the upper surface of the wing, we proceed with a more quantitative analysis. Recall that the lift increases while the LEV is attached to the wing [54, 55], C_z increases with α_e (as shown in Figure 2a) and depends mainly on the contribution from the pressure forces (i.e. normal forces). Then, it might be considered that the local separation of the LEV at a given spanwise wing section occurs when the contribution of c_n to the vertical force at that section peaks (and drops) before the maximum α_e is reached (at the mid-downstroke, $t/T = 0.25$).

In Figure 7a, the contribution of the local normal force coefficient to the vertical force

$$c_z^n(y_w, t) = \frac{1}{c} \int_0^c c_n(\xi, t) \, \mathbf{n} \cdot \mathbf{e}_z \mathrm{d}\xi, \tag{16}$$

is shown during the downstroke at two sections along the span ($y_w/b = 0.5$ and $y_w/b = 0.75$). Three cases are shown in the Figure, namely heaving (2W-Rinf), flapping (2W-R000) and an intermediate configuration (2W-R020). The corresponding flow in these two sections at mid-downstroke is shown in the middle and right panels of Figure 6, in the top, middle and bottom rows. For the heaving case, $c_z^n(y_w = 0.5b, t)$ peaks at $t/T \approx 0.2$, well before mid-downstroke. On the other hand, closer to the outer wing tip the peak of $c_z^n(y_w = 0.75b, t)$ occurs later, closer to the mid-downstroke. These observations suggest that the LEV separates first in the mid-span of the wing, and later closer to the wing tips. Interestingly, the behavior of the flapping case with $R = 0$ (2W-R000) is the opposite, suggesting that for this case the separation of the LEV starts closer to the wing tips. For the intermediate case, the peak of c_n^z is achieved roughly at the same time at both locations, $y_w = 0.5b$ and $y_w = 0.75b$. Overall, the results in Figure 7a seem to suggest that, as observed qualitatively in Figure 6, the location where the separation of the LEV occurs can be found closer to the outboard wing tip as R decreases.

To better characterize this behavior, the time to maximum c_z^n at each spanwise section, $t_{c_{z,max}^n}$, is shown in Figure 7b (i.e., the time when the separation of the LEV starts at each spanwise section). In agreement with the discussion of Figure 7a, the heaving case (2W-Rinf) shows a roughly uniform region around mid-span (i.e., $0.6 \lesssim y_w/c \lesssim 1.4$) where the LEV separation occurs at about $0.2T$. Note that the spanwise extension of this region roughly corresponds to that of the region with $\partial c_n/\partial x_w \approx 0$ in Figure 5 (highlighted with the red rectangle), and with the sizes of separated LEV that can be observed in the supplementary videos. As R decreases, the region where the maximum of c_z^n is attained first can be found closer to the outboard wing tip, consistently with the previous
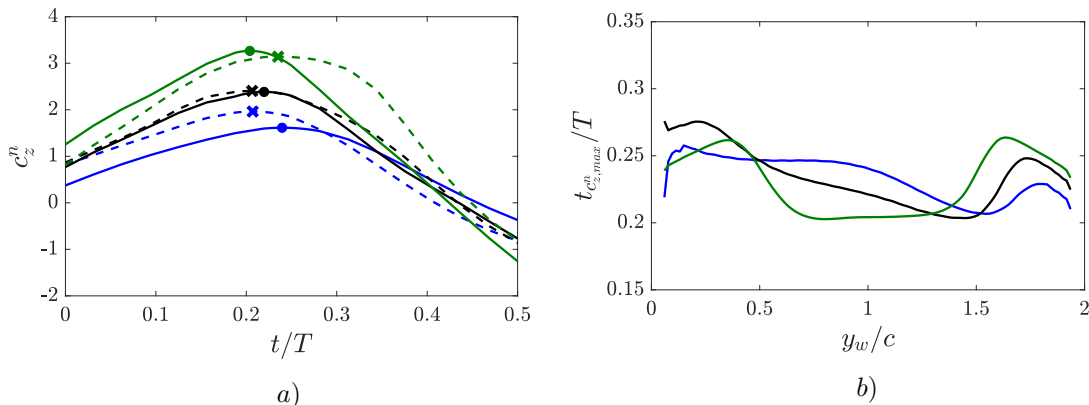
Figure 7: a) Contribution of the local normal force coefficient to the vertical force, $c_z^n(y_w, t)$. Two spanwise sections are considered, $y_w/b = 0.5$ (——) and $y_w/b = 0.75$ (---). b) Time to maximum c_z^n ($t_{c_{z,max}^n}$), plotted as a function of the spanwise coordinate of the wing (y_w). The cases represented in both Figures are 2W-R000 (——), 2W-R020 (——) and 2W-Rinf (——).

discussion. Moreover, for the case 2W-R000, the maximum of c_z^n in the region $y_w \lesssim 0.5b$ occurs at mid-downstroke, which could be interpreted as sections where the separation of the LEV is very weak (or inexistent).

4.4 Comparison with unsteady panel methods

While direct numerical simulations provide accurate predictions of the aerodynamic forces on flapping wings, their computational cost is extremely high for practical applications. It is therefore interesting to explore the ability of less expensive methods, as unsteady panel methods (UPMs) [56] to predict the aerodynamic forces on flapping wings. These methods are based in a potential description of the velocity field that assumes that the Reynolds number of the flow is sufficiently high, the flow is incompressible and the incoming free-stream is irrotational. Despite these strict assumptions, UPMs have been used by several authors to study flapping flight of birds and insects [57, 58, 59, 60], and some of the limitations of UPMs for the modeling of Micro Air Vehicles have been already discussed in the literature [61]. In this section, we report the aerodynamic forces obtained for the present configuration using the UPM of Arranz & Flores [62]. The results of the UPM are compared to the DNS results presented in the previous section, to evaluate the appropriateness of a UPM to model the aerodynamic forces in the present case.

The UPM of Arranz & Flores [62] uses an indirect formulation, discretizing the 3D surface of the wing with trapezoidal panels with uniform distributions of sources and doublets. The wake is allowed to move with the flow, adjusting the doublets in the panels shed into the wake at each timestep imposing the Kutta condition at the wing TE. After being shed, the intensity of the doublets in the wake panels remains constant. The interested reader can find further details in [62]. It should be noted that the present implementation of the UPM only considers a vortex sheet shed at the trailing edge, while other methods also consider a vortex sheet shed at the leading edge [60]. The latter strategy allows a certain level of modelling of the LEV, which is not available in the present implementation of the UPM. As discussed below, this will have a strong effect on the prediction of the suction force at the leading edge.

For the present calculations, the resolution is the same as in [62], discretizing the wings with $M_x \times M_y = 24 \times 32$ panels in each wing, and truncating the wake $12c$ downstream of the trailing edge. All configurations in Table 1 have been simulated, but for brevity only the cases 2W-R000, 2W-R020 and 2W-Rinf are discussed below.

For the comparison between the DNS and the UPM, and since viscous effects are absent in UPMs, only the contribution from the normal forces (C_z^n and C_x^n) are considered. These two quantities are displayed in Figure 8 as a function of time during one cycle, together with the lift and drag coefficients obtained with the UPM. Concerning the lift coefficient, Figure 8a, the
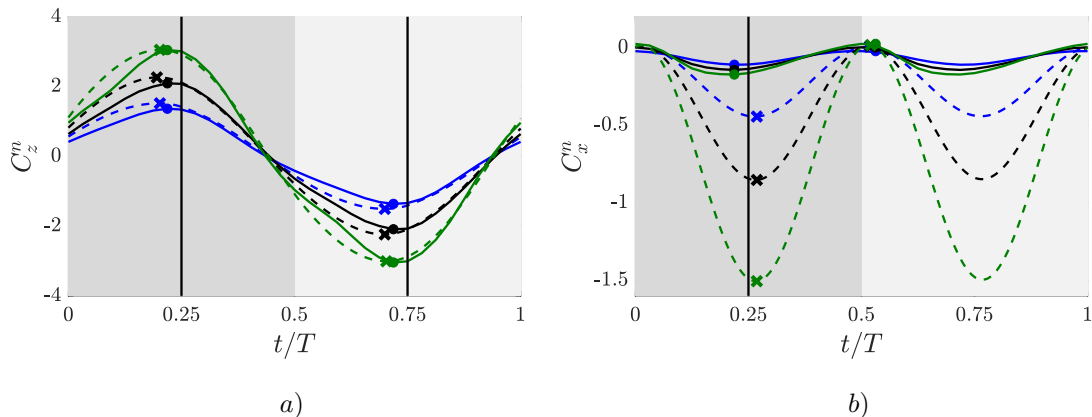
Figure 8: Normal force coefficients (a) C_z^n and (b) C_x^n of cases 2W-R000 (———), 2W-R020 (———) and 2W-Rinf (———) during one cycle. (———) lines represent DNS cases and (- - -) lines stand for 3D unsteady panel method simulations. Maximum and minimum values of the force coefficients are depicted with (●) for DNS simulations and with (✖) for 3D unsteady panel method simulations. Dark and light greys regions represent downstroke and upstroke motions respectively.

agreement between DNS and UPM is remarkable. Both the shape of the profile and the intensity of the peaks are well predicted by the UPM. On the contrary, the UPM fails to provide a good estimation of the drag coefficient, as shown in Figure 8b. While the peak thrust coefficient (due to normal forces) predicted by the DNS is small, $C_x^n \approx -0.15$ (see Figure 3a), a much larger value is predicted by the UPM, C_x^n between -0.5 and -1.5 depending on the case considered. Only during the stroke reversals, when the velocity of the wing due to the flapping motion is close to zero, both DNS and UPMs provide similar values for the drag coefficient. At that time instant, the UPM sheds a strong vortex into the wake [62], resulting in a vortical structure qualitatively similar to that observed in Figure 6, which seems to be correlated with the similarities observed in C_z^n between the UPM and the DNS.

The fact that C_z^n is well predicted by the UPM, but C_x^n is not, hints that the distribution of c_n in the DNS and UPMs are different. This is confirmed in Figure 9, which displays contours of c_n in the upper surface of the wing for 2W-Rinf and 2W-R000 at mid-downstroke. Figure 9 shows that, although the UPM captures qualitatively the spanwise changes in the force distribution, the chordwise distribution of c_n are very different for both 2W-Rinf and 2W-R000. Indeed, the UPM predicts a suction area (positive c_n) confined to a small region near the leading edge of the wing (note the saturation of the color scale in Figure 9b and d). However, the DNS data show larger suction regions, covering more than 2/3 of the wing surface (Figure 9a and c). Hence, while the maximum c_n for the DNS calculations of 2W-Rinf is $c_n \sim 4$, located at $x_w/c \sim 0.04$ and $y_w/c \sim 0.08$, the maximum in the UPM simulations is ten times larger ($c_n \sim 40$) and is reached at $x_w/c \sim 0.01$ and $y_w/c \sim 1.20$. A similar observation can be done for case 2W-R000. Note that this implies that the UPM shows a stronger suction peak closer to the leading edge, where the local $\mathbf{n}$ is reasonably aligned with $\mathbf{e}_x$, explaining the difference of more than one order of magnitude in the C_x^n computed from DNS and UPM (see Figure 8b). Although not shown, the differences between DNS and UPM in the c_n distribution on the lower surface are less relevant.

It seems reasonable to assume that the differences in the c_n distributions between both methods are related to the presence of the LEV in the DNS (and its absence in our implementation of the UPM). Indeed, the presence of the LEV in the DNS explains the broad suction peak near the leading edge, while in the UPM the need for an attached boundary layer at the leading edge results in a very strong suction peak close to $x_w \approx 0$. A bit more puzzling is the good agreement in terms of C_z^n between UPM and DNS, where the former is able to produce a spanwise distribution of bound circulation compatible with the overall pressure difference between suction and pressure surfaces in the DNS. It should be noted that the agreement in C_z^n between the DNS and the UPM in Figure 8 is worse during the first half of the stroke than during the second half. Interestingly, during the first half of the stroke the LEV is being developed, while it is shed into the wake shortly
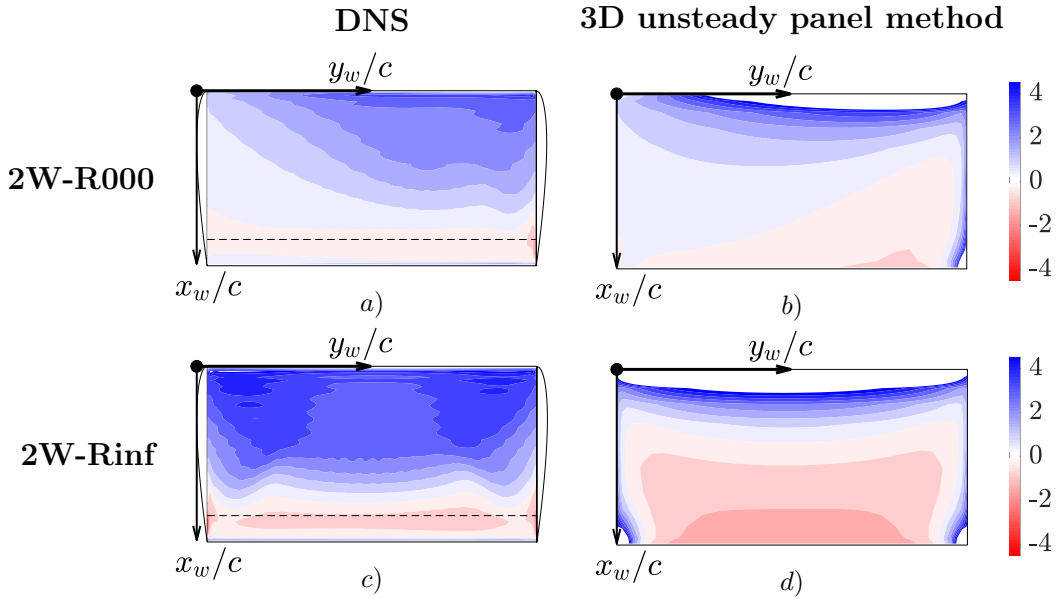
16

Figure 9: Normal force coefficient (c_n) at the mid-downstroke ($t/T = 0.25$), on the upper surface of the wing. (a) and (b), case 2W-R000. (c) and (d), case 2W-Rinf. Panels (a) and (c) show DNS results. Panels (b) and (d) show UPM results.

after the mid-stroke (see the videos in the supplementary material).

Finally, it is interesting to note that Moriche et al. [33] reported that in 2D flapping airfoils in a viscous flow the force due to circulatory effects is roughly perpendicular to the chord of the airfoil. A model for this phenomenon was proposed rather early by Polhamus [63] in the framework of the separated leading edge vortices appearing on delta wings. This suggests that it should be possible to modify simple UPMs like the one used here to keep the component of the force perpendicular to the wing, discarding the component of the force along the chord (i.e. C_x^n in the present case).

5   Conclusions

We have presented a series of direct numerical simulations of flapping wings in forward flight at Reynolds number $Re = 500$ and reduced frequency $k = 1$. The calculations were performed by solving the Navier-Stokes equations using an immersed boundary method, prescribing the motion of the wings. We have varied the radius of flapping motion, R, so that when $R \to \infty$ the wing is in heaving motion, and when $R = 0$ the wing is flapping with respect to the inboard wing tip. Due to the symmetry of the prescribed motion, the downstroke and upstroke are equivalent and therefore we have only analyzed the downstroke in detail.

Keeping fixed the vertical displacement of the outboard wing tip, the peak aerodynamic force decreases with R, so that the force is maximum for the heaving wing. Note that for the heaving case, all wing sections are subject to the same effective angle of attack. However, when decreasing R, the effective angle of attack near the outboard wing tip is roughly the same as in the heaving wing case, but its value decreases towards the inboard wing tip, resulting in a lower peak force. In order to confirm that the governing parameter is the effective angle of attack, we have performed an additional heaving wing simulation with a smaller vertical displacement. The aerodynamic forces obtained in this case were very similar to those obtained in the flapping wing simulation with the same averaged effective angle of attack.

We have decomposed the force in the tangential and normal components and we have analyzed their corresponding contributions to the vertical force (lift) and the streamwise force (drag-thrust). While the vertical force is dominated by normal forces, the streamwise force is the result of a competition between normal contributions that produce thrust and tangential contributions that produce drag. For the tangential contributions, it has been found that the differences between the configurations with different radius of flapping motion are linked to the position of the stagnation
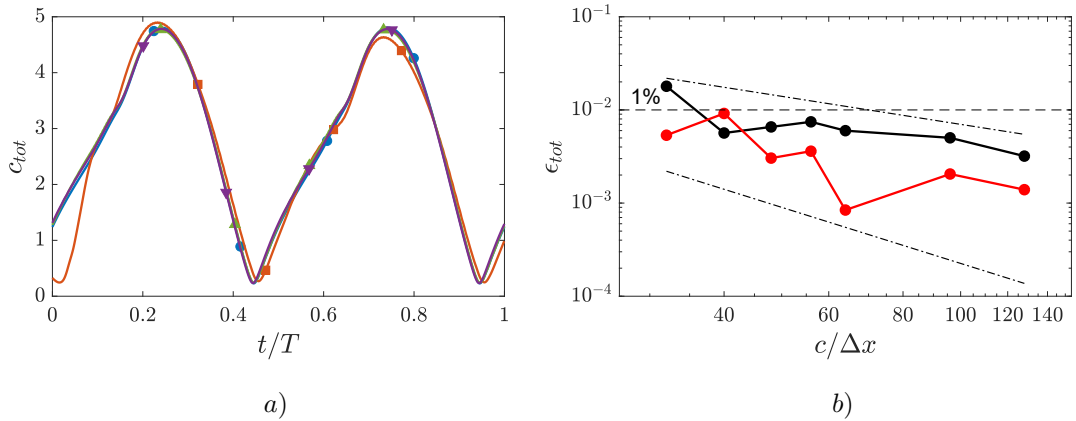
Figure 10: *a)* Total force coefficient c_{tot} during one cycle for 2D cases performed with resolutions $c/\Delta x = 32$ (■—■), $c/\Delta x = 56$ (▲—▲), $c/\Delta x = 96$ (▼—▼) and $c/\Delta x = 192$ (●—●). *b)* Errors of c_{tot} (ϵ_{tot}) obtained in mean (——) and rms (——). The black dash-dotted lines have logarithmic slopes -1 and -2.

point near the leading edge, which is controlled by the local effective angle of attack. The normal contributions to the vertical force have been analyzed using the distribution of the force per unit area, which presents lower suction in the upper surface near the inboard tip when decreasing R.

It has been shown that the flow over the wings is rather complex, with the presence of a leading edge vortex and tip vortices, which interact and are shed into the wake forming ring-like structures. The rings are clearly visible for the cases with large R. For smaller R, the displacement of the inboard wing tip decreases and the inboard wing tip vortices become less intense, disappearing when $R = 0$. For this case, the vortical structures shed into the wake are half-rings. We have analyzed qualitatively and quantitatively the LEV separation, and how it correlates with the normal force distribution on the wing. We have found that the spanwise location where the separation of the LEV occurs depends on the radius of flapping motion. For the heaving case, the LEV separates earlier near the mid span, while for the flapping case, the LEV separates earlier near the outer wing tip.

Finally, we have explored the ability of unsteady potential flow methods for predicting the aerodynamic forces on flapping wings. When comparing to the DNS data, we have found a very good agreement for the lift coefficient and a poor prediction of the drag coefficient. Even if the lift coefficient is well predicted, it has been shown that the force distribution on the surface of the wing obtained from the unsteady potential flow method is very different to that obtained in the DNS. Thus, these methods should not be used for the prediction of other quantities of aerodynamic interest like the pitching moment coefficient.

Appendix: Grid refinement study

In this section we present the grid refinement study carried out to select the resolution used in the simulations. This study is performed in 2D for its lower computational cost. Note that the resolution requirements of the 2D simulations are expected to be similar to those of the 3D configurations, since the geometry of the wing is somewhat smoother in the spanwise direction than in the streamwise and vertical directions (see Figures 1*c*, *d* and *e*).

We perform 2D simulations of a heaving NACA0012 airfoil, with heaving amplitude $h_0 = c$, Reynolds number $Re = 500$ and reduced frequency $k = 1$, varying the resolution from $c/\Delta x = 32$ to $c/\Delta x = 192$. The time step Δt is varied accordingly, keeping the same CFL number for all

cases (lower than 0.3). The convergence is evaluated in terms of the aerodynamic force, using as reference the results of the case with the highest resolution ($c/\Delta x = 192$). The time evolution of the total force coefficient,

$$c_{tot} = \frac{|\boldsymbol{F}|}{\frac{1}{2}\rho u_\infty^2 c}, \tag{17}$$

of four of the simulations is reported in Figure 10a. In the previous expression $\boldsymbol{F}$, is the total aerodynamic force on the airfoil. While some deviations are observed for the resolution $c/\Delta x = 32$ with respect to the reference case, the results of the simulation with $c/\Delta x = 56$ are very close to those of the reference case. In order to quantify these differences, Figure 10b shows the errors in the mean and rms of the force

$$\epsilon_{tot}^{\text{mean}}(r) = \frac{|\overline{c}_{tot\,r} - \overline{c}_{tot\,192}|}{c'_{tot\,192}}, \tag{18}$$

$$\epsilon_{tot}^{\text{rms}}(r) = \frac{|c'_{tot\,r} - c'_{tot\,192}|}{c'_{tot\,192}}, \tag{19}$$

where an overline denotes the time-average, the prime denotes the root-mean-square of the fluctuation and r is the resolution of each case. As expected, the errors decrease with increasing resolution. Taking into account a compromise between the computational cost and the accuracy of the results, a resolution of $c/\Delta x = 56$ is selected for the simulations presented in this article. With this resolution, the errors for both mean and rms of the forces are smaller than 1%.

References

[1] C. P. Ellington. The novel aerodynamics of insect flight: applications to micro-air vehicles. *J. Exp. Biol.*, 202(23):3439–3448, 1999.

[2] Z. J. Wang. Dissecting insect flight. *Annu. Rev. Fluid Mech.*, 37:183–210, 2005.

[3] W. Shyy, H. Aono, C. K. Kang, and H. Liu. *An introduction to flapping wing aerodynamics.* Cambridge University Press, 2013.

[4] C. P. Ellington. The aerodynamics of hovering insect flight. IV. Aerodynamic mechanisms. *Philos. Trans. R. Soc. Lond., B, Biol. Sci.*, 305(1122):79–113, 1984.

[5] J.M. Anderson, K. Streitlien, K. S. Barret, and M. S. Triantafyllou. Oscillating foils of high propulsive efficiency. *J. Fluid Mech.*, 360:41–72, 1998.

[6] G. C. Lewin and H. Haj-Hariri. Modelling thrust generation of a two-dimensional heaving airfoil in a viscous flow. *J. Fluid Mech.*, 492:339–362, 2003.

[7] D. A. Read, F. S. Hover, and M. S. Triantafyllou. Forces on oscillating foils for propulsion and maneuvering. *J. Fluids Struct.*, 17(1):163–183, 2003.

[8] Y. S. Baik, L. P. Bernal, K. Granlund, and M. V. Ol. Unsteady force generation and vortex dynamics of pitching and plunging aerofoils. *J. Fluid Mech.*, 709:37–68, 2012.

[9] J. Choi, T. Colonius, and D. R. Williams. Surging and plunging oscillations of an airfoil at low Reynolds number. *J. Fluid Mech.*, 763:237–253, 2015.

[10] A. Martín-Alcántara, R. Fernández Feria, and E. Sanmiguel-Rojas. Vortex flow structures and interactions for the optimum thrust efficiency of a heaving airfoil at different mean angles of attack. *Phys. Fluids*, 27:073602, 2015.

[11] M. Y. Zakaria, H. E. Taha, and M. R. Hajj. Measurement and modeling of lift enhancement on plunging airfoils: A frequency response approach. *J. Fluids Struct.*, 69:187–208, 2017.

[12] W. B. Dickson and M. H. Dickinson. The effect of advance ratio on the aerodynamics of revolving wings. *J. Exp. Biol.*, 207(24):4269–4281, 2004.

[13] D. Lentink and M. H. Dickinson. Rotational accelerations stabilize leading edge vortices on revolving fly wings. *J. Exp. Biol.*, 212(16):2705–2719, 2009.

[14] T. Jardin and L. David. Spanwise gradients in flow speed help stabilize leading-edge vortices on revolving wings. *Phys. Rev. E*, 90(1):013011, 2014.

[15] Y. J. Lee, K. B. Lua, and T. T. Lim. Aspect ratio effects on revolving wings with Rossby number consideration. *Bioinspir. & Biomim.*, 11(5):056013, 2016.

[16] I. Gursul and D. Cleaver. Plunging oscillations of airfoils and wings: Progress, opportunities, and challenges. *AIAA J.*, 2018. in press.

[17] H. Dong, R. Mittal, and F. M. Najjar. Wake topology and hydrodynamic performance of low-aspect-ratio flapping foils. *J. Fluid Mech.*, 566:309–343, 2006.

[18] J.E. Guerrero. Wake signature and Strouhal number dependence of finite-span flapping wings. *J. Bionic Eng.*, 7:S109–S122, 2010.

[19] F. M. Bos, B. W. van Oudheusden, and H. Bijl. Wing performance and 3-D vortical structure formation in flapping flight. *J. Fluids Struct.*, 42:130–151, 2013.

[20] H. Nagai, K. Isogai, T. Fujimoto, and T. Hayase. Experimental and numerical study of forward flight aerodynamics of insect flapping wing. *AIAA J.*, 47(3):730, 2009.

[21] N. Yokoyama, K. Senda, M. Iima, and N. Hirai. Aerodynamic forces and vortical structures in flapping butterfly's forward flight. *Phys. Fluids*, 25(2):021902, 2013.

[22] L. Zheng, T.L. Hedrick, and R. Mittal. Time-varying wing-twist improves aerodynamic efficiency of forward flight in butterflies. *PLOS One*, 8(1):e53060, 2013.

[23] G. Liu, H. Dong, and C. Li. Vortex dynamics and new lift enhancement mechanism of wing–body interaction in insect forward flight. *J. Fluid Mech.*, 795:634–651, 2016.

[24] J. Song, B. W. Tobalske, D. R. Powers, T. L. Hedrick, and H Luo. Three-dimensional simulation for fast forward flight of a calliope hummingbird. *Roy. Soc. Open Sci.*, 3(6):160230, 2016.

[25] K. Viswanath, K. Nagendra, J. Cotter, M. Frauenthal, and D.K. Tafti. Straight-line climbing flight aerodynamics of a fruit bat. *Phys. Fluids*, 26(2):604, 2014.

[26] S. Deng, M. Percin, B. W. van Oudheusden, H. Bijl, B. Remes, and T. Xiao. Numerical simulation of a flexible x-wing flapping-wing micro air vehicle. *AIAA J.*, 55(7):2295–2306, 2017.

[27] M. Moriche, E. Hernández-Hurtado, O. Flores, and M. García-Villalba. Numerical simulation of the flow around a flapping-wing micro air vehicle in free flight. Proc. Inst. Mech. Eng. G: J. Aerospace Eng., in press, 2018.

[28] K. Isogai, Y. Shinmoto, and Y. Watanabe. Effects of dynamic stall on propulsive efficiency and thrust of flapping airfoil. *AIAA J.*, 37(10):1145–1151, 1999.

[29] J. Young and J. C. S. Lai. Oscillation frequency and amplitude effects on the wake of a plunging airfoil. *AIAA J.*, 42(10):2042–2052, 2004.

[30] M. Uhlmann. An immersed boundary method with direct forcing for the simulation of particulate flows. *J. Comput. Phys.*, 209(2):448–476, 2005.

[31] M. Moriche, O. Flores, and M. García-Villalba. Three-dimensional instabilities in the wake of a flapping wing at low Reynolds number. *Int. J. Heat Fluid Flow*, 62:44–55, 2016.

[32] M. Moriche. *A numerical study on the aerodynamic forces and the wake stability of flapping flight at low Reynolds number.* PhD thesis, Univ. Carlos III Madrid, 2017.

[33] M. Moriche, O. Flores, and M. García-Villalba. On the aerodynamic forces on heaving and pitching airfoils at low Reynolds number. *J. Fluid Mech.*, 828:395–423, 2017.

[34] W. R. Sears. Some recent developments in airfoil theory. *J. Aeronautical Sci.*, 23(5):490–499, 1956.

[35] P. Trizila, C.-K. Kang, H. Aono, W. Shyy, and M. Visbal. Low-Reynolds-number aerodynamics of a flapping rigid flat plate. *AIAA J.*, 49(4):806–823, 2011.

[36] C.-K. Kang, H. Aono, Y. Sik Baik, L. P. Bernal, and W. Shyy. Fluid dynamics of pitching and plunging flat plate at intermediate Reynolds numbers. *AIAA J.*, 51(2):315–329, 2012.

[37] M. Visbal, T. O. Yilmaz, and D. Rockwell. Three-dimensional vortex formation on a heaving low-aspect-ratio wing: Computations and experiments. *J. Fluids Struct.*, 38:58–76, 2013.

[38] K. Taira and T. Colonius. Three-dimensional flows around low-aspect-ratio flat-plate wings at low Reynolds numbers. *J. Fluid Mech.*, 623:187–207, 2009.

[39] C. Chan-Braun, M. García-Villalba, and M. Uhlmann. Force and torque acting on particles in a transitionally rough open-channel flow. *J. Fluid Mech.*, 684:441–474, 2011.

[40] G. Arranz, M. Moriche, M. Uhlmann, O. Flores, and M. García-Villalba. Kinematics and dynamics of the auto-rotation of a model winged seed. *Bioinspir. Biomim.*, 13:036011, 2018.

[41] A. P. Maertens and G. D. Weymouth. Accurate Cartesian-grid simulations of near-body flows at intermediate Reynolds numbers. *Comput. Meth. Appl. Mech. Eng.*, 283:106–129, 2015.

[42] C. S. Peskin. The immersed boundary method. *Acta Numer.*, 11:479–517, 2002.

[43] J. C. R. Hunt, A. A. Wray, and P. Moin. Eddies, streams, and convergence zones in turbulent flows. *Center For Turbulence Research*, Report CTR-S88, 1988.

[44] K. D. Von Ellenrieder, K. Parker, and J. Soria. Flow structures behind a heaving and pitching finite-span wing. *J. Fluid Mech.*, 490:129–138, 2003.

[45] M.S. Triantafyllou, A.H. Techet, and F.S. Hover. Review of experimental work in biomimetic foils. *IEEE J. Ocean. Eng.*, 29(3):585–594, 2004.

[46] T. Jardin, A. Farcy, and L. David. Three-dimensional effects in hovering flapping flight. *J. Fluid Mech.*, 702:102–125, 2012.

[47] M. Bross and D. Rockwell. Flow structure on a simultaneously pitching and rotating wing. *J. Fluid Mech.*, 756:354–383, 2014.

[48] Z. R. Carr, C. Chen, and M. J. Ringuette. Finite-span rotating wings: three-dimensional vortex formation and variations with aspect ratio. *Exp. Fluids*, 54(2):1444, 2013.

[49] R. R. Harbig, J. Sheridan, and M. C. Thompson. The role of advance ratio and aspect ratio in determining leading-edge vortex stability for flapping flight. *J. Fluid Mech.*, 751:71–105, 2014.

[50] M. R. Visbal. Three-dimensional flow structure on a heaving low-aspect-ratio wing. AIAA Paper 2011-219, 2011.

[51] M. R. Visbal. Flow structure and unsteady loading over a pitching and perching low-aspect-ratio wing. AIAA Paper 2012-3279, 2012.

[52] Y. H. Chen and M. Skote. Study of lift enhancing mechanisms via comparison of two distinct flapping patterns in the dragonfly sympetrum flaveolum. *Phys. Fluids*, 27(3):033604, 2015.

[53] J. M. Birch and M. H. Dickinson. Spanwise flow and the attachment of the leading-edge vortex on insect wings. *Nature*, 412(6848):729–733, 2001.

[54] PG Saffman and JS Sheffield. Flow over a wing with an attached free vortex. *Stud. Appl. Maths*, 57(2):107–117, 1977.

[55] C. W. Pitt Ford and H. Babinsky. Lift and the leading-edge vortex. *J. Fluid Mech.*, 720:280–313, 2013.

[56] J. Katz and A. Plotkin. *Low-speed aerodynamics*. Cambridge Univ. Press, 2001.

[57] M. S. Vest and J. Katz. Unsteady aerodynamic model of flapping wings. *AIAA J.*, 34(7):1435–1440, 1996.

[58] L. N. Long and T. E. Fritz. Object-oriented unsteady vortex lattice method for flapping flight. *J. Aircraft*, 41(6):1275–1290, 2004.

[59] P.-O. Persson, D. J. Willis, and J. Peraire. Numerical simulation of flapping wings using a panel method and a high-order Navier–Stokes solver. *Int. J. Num. Meth. Eng.*, 89(10):1296–1316, 2012.

[60] B. A. Roccia, S. Preidikman, J. C. Massa, and D. T. Mook. Modified unsteady vortex-lattice method to study flapping wings in hover flight. *AIAA J.*, 51(11):2628–2642, 2013.

[61] R. Ansari, R. Zbikowski, and K. Knowles. Aerodynamic modelling of insect-like flapping flight for micro air vehicles. *Prog. Aerospace Sci.*, 42:129–172, 2006.

[62] G. Arranz and O. Flores. Thrust generation in heaving and flapping wings in forward flight. AIAA Paper 2016-3556, 2016.

[63] E. C. Polhamus. A concept of the vortex lift of sharp-edge delta wings based on a leading-edge-suction analogy. NASA Tech Note D-3767, 1966.